

Honeycomb-like Porous Crystalline Hetero-electrocatalyst for Efficient Electrocatalytic CO₂ Reduction

Yi-Lu Yang^{1‡}, Yi-Rong Wang^{1‡}, Long-Zhang Dong^{1‡}, Qi Li², Lei Zhang¹, Jie Zhou¹, Sheng-Nan Sun¹, Hui-Min Ding², Yifa Chen^{1*}, Shun-Li Li¹ & Ya-Qian Lan¹

¹Y.-L. Y., Y.-R. W., L.-Z. D., Q. L., L. Z., J. Z., S.-N. S., H.-M. D., Prof. Y. C., Prof. S.-L. L., and Prof. Y. -Q. L National and Local Joint Engineering Research Center of MPTES in High Energy and Safety LIBs, Engineering Research Center of MTEES (Ministry of Education), Key Lab. of ETESPG(GHEI), School of Chemistry, South China Normal University, Guangzhou, 510006, P. R. China.

E-mail: chyf927821@163.com

²Q. L. and H.-M. D.

School of Chemistry and Materials Science, Nanjing Normal University, Nanjing, 210023, P. R. China.

[‡]Yi-Lu Yang, Yi-Rong Wang and Long-Zhang Dong contributed equally to this work.

Keywords: Electrocatalytic CO₂ Reduction • MOF@COF Hetero-structures • Honeycomb-like • Methane

Abstract

Porous hetero-structure electrocatalysts with multi-functionality and synergistic effect have much benefit for efficient electrocatalytic CO₂ reduction reaction (CO₂RR), yet it still remains a daunting challenge to explore covalent-organic frameworks (COFs) and metal-organic frameworks (MOFs) based hetero-structures in this field. Here, we have synthesized a series of honeycomb-like porous

This article has been accepted for publication and undergone full peer review but has not been through the copyediting, typesetting, pagination and proofreading process, which may lead to differences between this version and the [Version of Record](#). Please cite this article as doi: [10.1002/adma.202206706](https://doi.org/10.1002/adma.202206706).

This article is protected by copyright. All rights reserved.

crystalline hetero-electrocatalysts (MCH-X, X = 1-4, X stands for the numbered sample obtained from different MOFs doses in MCH synthesis) and successfully applied them in electrocatalytic CO₂RR. The specially designed hetero-structures with integrated porous MOF-template and ultrathin COF-coating enable efficient CO₂ adsorption/activation and conversion into CH₄. Best of them, the MCH-3 showed greatly inhibited H₂ evolution, excellent current density (-398.1 mA cm⁻²), and superior FE_{CH₄} (76.7%) to physical mixture (38.0%), MOF@COF without honeycomb-like morphology (47.7%), bare COF (37.5%) and MOF (15.9%) at -1.0 V. Based on the DFT calculations and various characterizations, the vital roles of MOF in facilitating CO₂ adsorption/activation, stabilizing intermediates, and conquering the energy barrier of rate-determining step have been intensively studied.

1. Introduction

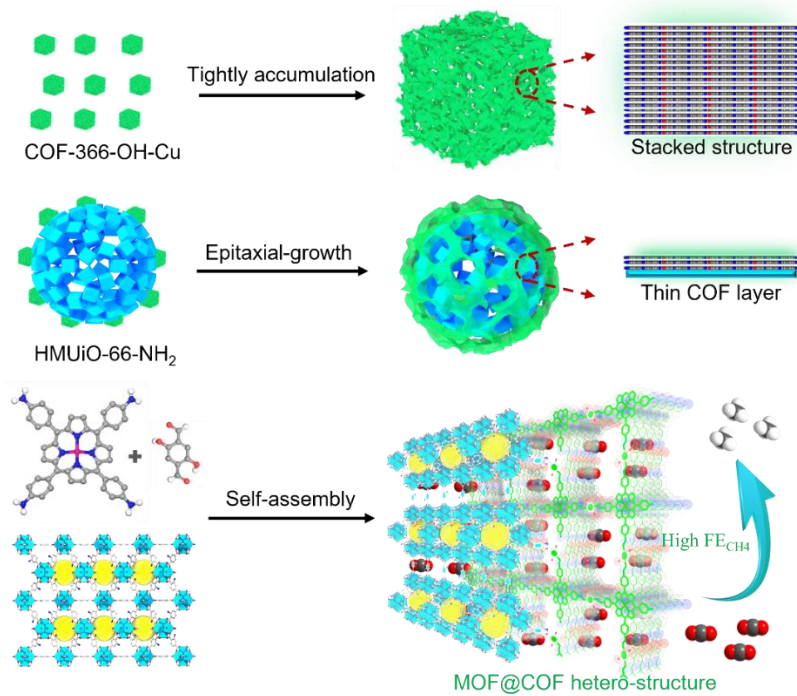
Covalent organic frameworks (COFs), as a new category of porous crystalline materials consisting of light elements, are extended through covalent bonds and presented as 2D or 3D frameworks.^[1,2] They have been exploded as salient materials around the world due to their unique properties like high crystallinity, permanent porosity, excellent stability, low density and tunable structures,^[3,4] which underpin their potential applications in proton conduction,^[5,6] catalysis,^[7,8] gas storage/separation^[9,10] and energy storage,^[11,12] etc. During past decades, COFs are regarded as ideal candidates for electrocatalytic CO₂ reduction reaction (CO₂RR) due to their advantages that might be much beneficial for CO₂ adsorption/diffusion, imparting of functional units and serving as platforms for structure-activity investigation.^[13-15] In general, they are applied by consciously introducing functional units like bipyridine, porphyrin, and phthalocyanine into COF skeletons to rivet metal ions for electrocatalytic CO₂RR.^[16-18] Albeit there has been considerable advancement in electrocatalytic CO₂RR, the generally applied forms are mostly based on single COF component, which would be restricted by the insulated crystalline nature and the lack in function diversity.^[19,20] In addition, their CO₂RR activity are mostly limited in two-electron transferred products like CO and the efficient production of higher-value products (e.g., CH₄, C₂H₄, and ethanol, etc.) involving multiple proton-coupled electron transfer (PCET) is still rare.^[21,22] Therefore, the introduction of additional functional components to synthesize multi-component COF-based hybrid materials would be much desired to fulfill the unmet functionality by itself, and further extend the application scope of COFs in electrocatalytic CO₂RR.

Metal-organic frameworks (MOFs), another class of porous frameworks, have been reported to be good candidates to construct hybrids with COFs.^[23,24] Since the first report of their hybrid materials in 2016, it has attracted much attention and evolved as interesting platform for diverse applications.^[25] Despite the many common features, there are still quite notable differences and complementarity for COFs and MOFs, and the combination of them might inherit plenty of their own advantages to mitigate their inadequacies.^[26-29] In recent years, the preparation approaches of MOF@COF hybrid materials are mainly based on: 1) the construction of amino- or aldehyde-functionalized MOFs as cores and COFs are then grown on the surface of MOFs through the covalent linking process^[30-34] and 2) direct growth of COFs on MOFs (without amino or aldehyde groups) through π - π stacking interaction.^[35-38] However, the reported synthetic methodology for their hybrids generally results in simple combination of MOFs and COFs as forms like core-shell or hetero-structures, and they still have intrinsic deficiencies like the wrapped inner component with buried active sites, the lack in interfacial effect or synergistic mechanism study, etc. Even so, the applications of MOF@COF hetero-structures in electrocatalytic CO₂RR have been rarely reported as far as we know. Theoretically speaking, it would be especially attractive to investigate their potentials in efficient generation of higher-value products (e.g., CH₄, C₂H₄, and ethanol, etc.), in which MOFs possessing synergistic interaction with COFs can serve as the auxiliary to boost CO₂RR performance. Nonetheless, it is still a grand challenge to design such powerful MOF@COF hybrid materials as efficient CO₂RR electrocatalysts to enrich the application forms of them in this area.

As a proof-of-concept, we propose the self-assembly of honeycomb-like MOFs and Cu-porphyrin based COFs to construct MOF@COF hetero-structures so as to verify the feasibility of this inference (**Scheme 1**). The specific considerations are as follows: 1) the specially designed honeycomb-like MOFs with tremendous mesopores could serve as porous templates to boost the interface interaction with COFs and greatly expose the catalytic sites, which would be superior to the commonly stacked structure by COF itself;^[39-42] 2) Cu-porphyrin based COFs with catalytically active Cu-N₄ centers as ultrathin coating could efficiently converse CO₂ into value-added products^[43,44] and 3) the successful combination of them would provide ideal platforms for the investigation of hybrid engineering and synergistic electrocatalytic CO₂RR mechanism that are conducive to a deeper understanding of structure-activity relationships.^[44-46] From the above we deduce that honeycomb-

like MOF@COF hetero-structures will probably be promising candidates to enhance the electrocatalytic CO₂RR efficiency, while the assembly of this type of catalytic structure model is still hard and rarely reported.

Herein, we have prepared a series of honeycomb-like porous crystalline hetero-electrocatalysts (MCH-X, X = 1-4, X stands for the numbered sample obtained from different MOFs doses in MCH synthesis) through an epitaxial growth strategy (**Scheme 1**). Interestingly, the obtained hetero-structures integrated from porous MOF-template and ultrathin COF-coating possess unique honeycomb-like morphology, fully exposed active-sites, and abundant open channels that enable efficient CO₂ adsorption/activation and conversion into CH₄ (**Scheme 1**). Best of them, the MCH-3 showed greatly inhibited hydrogen evolution and much higher FE_{CH₄} (76.7%) than physical mixture (38.0%), MOF@COF without honeycomb-like hetero-structure (47.7%), bare COF (37.5%) and MOF (15.9%) at -1.0 V, revealing the superiority of the unique architecture in electrocatalytic CO₂RR. Noteworthy, the FE_{CH₄} of MCH-3 keeps ~70% over a wide potential range from -0.9 V to -1.1 V. Moreover, based on the DFT calculations and various characterizations, the vital roles of MOF in facilitating CO₂ adsorption/activation, stabilizing intermediates, and conquering the energy barrier of rate-determining step have been intensively studied. This is the first example of MOF@COF hetero-structures that can be applied in efficient CO₂RR to CH₄, which would also expedite the development of porous hybrid materials in this field.



Scheme 1. Schematic illustration of the formation and advantages of honeycomb-like MOF@COF hetero-structures (MCH-X, X = 1-4) in electrocatalytic CO₂RR.

2. Results

2.1. Synthesis and Characterization of MCH-X (X = 1-4)

For the syntheses of honeycomb-like MOF@COF hetero-structures (MCH-X, X = 1-4), HMUiO-66-NH₂ (HM stands for honeycomb-like MOF or hierarchically mesoporous) as the porous template was pre-synthesized followed by the in-situ growth of COF-366-OH-Cu on its surface (**Scheme 1**).^[47] UiO-66-NH₂ features a crystalline structure constituted by hexameric Zr₆O₃₂ units, in which six Zr atoms define a regular octahedron with triangular faces alternatively contain μ₃-O and μ₃-OH capping groups (**Figure S1a, b**).^[48] The octahedra are linked through 12 2-aminoterephthalate ligand molecules, thus defining two types of cages: a supertetrahedron and a superoctahedron. Specifically, the -NH₂ functional groups on the surface of HMUiO-66-NH₂ can in-situ generate covalent bond with

2,5-dihydroxyterephthalaldehyde (DHA) and further synthesize COF-366-OH-Cu on the surface, thus producing powerful MOF@COF hetero-structures (**Figure S2**). COF-366-Cu is a kind of 2D COF that is constructed by tetra(p-aminophenyl)porphyrin (Cu-TAPP) and DHA, in which the π - π stacking distance between COF layers is 3.8-4.4 Å (**Figure S1c, d**).^[42]

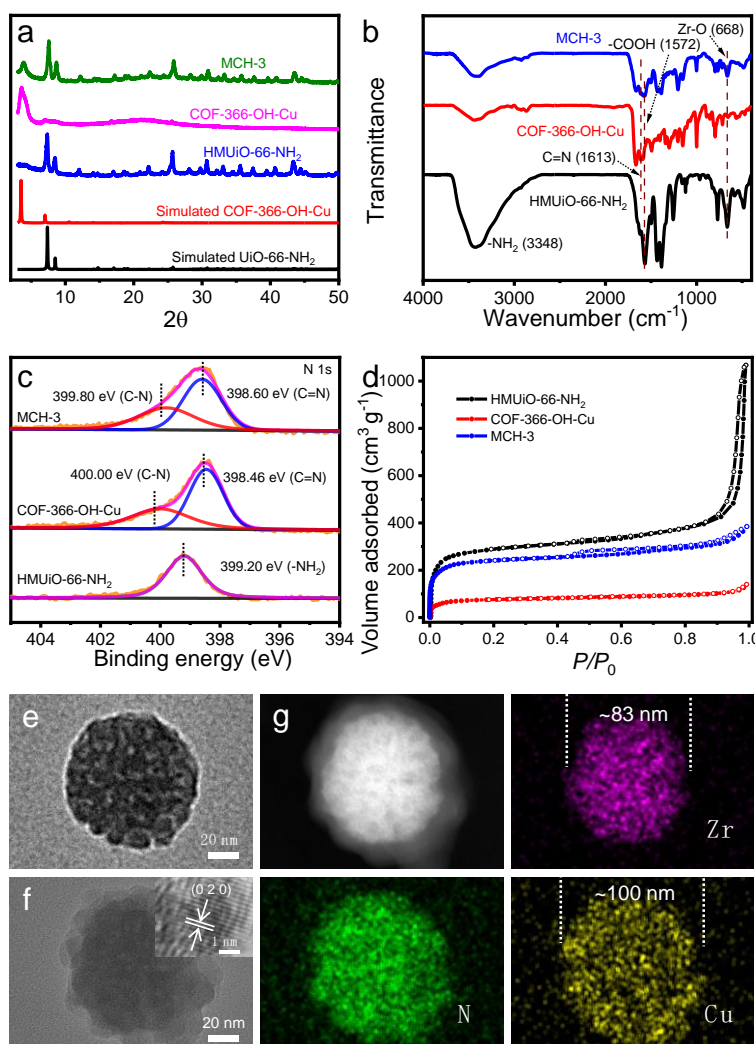


Figure 1. The characterization of MCH-3. (a) The PXRD patterns of MCH-3. (b) The FT-IR spectra of HMUIO-66-NH₂, COF-366-OH-Cu and MCH-3. (c) Survey scan XPS profiles of N 1s. (d) N₂ sorption curves measured at 77 K. (e) The TEM image of HMUIO-66-NH₂. (f) The TEM and HRTEM (inset) images of MCH-3 (the lattice spacing is 1.98 nm). (g) HAADF-STEM and elemental mapping images of MCH-3.

Interestingly, MCH-X ($X = 1-4$) could be achieved by tuning the different addition amounts of HMUiO-66-NH₂ into the COF synthetic system (detail see Methods). The obtained materials were firstly characterized by powder X-ray diffraction (PXRD) and Fourier transform infrared spectroscopy (FT-IR) tests (**Figure 1a**, **Figure S3 and S4**). Taking MCH-3 as an example, the strong peak at 3.4° is assigned to (1 0 0) crystal facet of COF-366-OH-Cu and the peaks at 7.3° and 8.5° are attributed to HMUiO-66-NH₂ in the PXRD tests, respectively, implying the co-existence of them (**Figure 1a**). Similar results have also been detected in MCH-X ($X = 1, 2$ and 4) (**Figure S3**).^[42,47] With the increased addition amount of HMUiO-66-NH₂ in the COF synthetic system, the characteristic peak intensity of HMUiO-66-NH₂ apparently increases from MCH-1 to MCH-4 (**Figure S3**). In the FT-IR spectrum, the appeared C=N stretching vibration at 1613 cm⁻¹ suggests the formation of imine linkage, indicating the successful synthesis of COF-366-OH-Cu in MCH-3 through Schiff base reaction (**Figure 1b**).^[43] The peak at 668 cm⁻¹ and 1572 cm⁻¹ are ascribed to the Zr-O bond and -COOH group, respectively, which can be both detected in HMUiO-66-NH₂ and MCH-3 (**Figure 1b**).^[45] This result suggests the existence of HMUiO-66-NH₂ in MCH-3. Furthermore, X-ray photoelectron spectroscopy (XPS) measurements have been conducted to determine HMUiO-66-NH₂, COF-366-OH-Cu and MCH-3 (**Figure S5**). The observed binding energy of 934.36 eV and 954.11 eV are ascribed to Cu 2p_{3/2} and Cu 2p_{1/2} in MCH-3, respectively, revealing the remained bivalent state of Cu in MCH-3 (**Figure S6b, d**).^[43] Besides, the peaks of 182.74 eV and 185.17 eV belong to Zr 3d_{5/2} and Zr 3d_{3/2}, respectively, suggesting the tetravalent state of Zr (**Figure S6**).^[45] The C 1s peak can be deconvoluted into three peaks that are ascribed to C-C (284.60 eV), C=O (288.70 eV), and C-O (286.10 eV) bonds, in which the C=O bond is dramatically decreased after COF-366-OH-Cu coating when compared MCH-3 with HMUiO-66-NH₂ (**Figure S6e**).^[46,51] For N 1s, the disappearance of -NH₂ (399.20 eV) groups in HMUiO-66-NH₂ and emergence of C=N bonds (398.60 eV) in MCH-3 imply the formation of covalent bond during the in-situ COF-366-OH-Cu synthesis process on HMUiO-66-NH₂ (**Figure 1c**).^[45]

Furthermore, scanning electron microscopy (SEM) and transmission electron microscopy (TEM) measurements have been performed to test the morphology. For HMUiO-66-NH₂, it displays honeycomb-like nano-spheres (size, 80-90 nm) with a large amount of uniform and accessible pores that can be directly observed in the sample (**Figure 1e**). After the coating of COF-366-OH-Cu, MCH-X

(X = 1-4) all exhibit remained honeycomb-like morphology in the TEM measurements (**Figure 2**). Taking MCH-3 as an example, it displays honeycomb-like hetero-structure morphology with ~100 nm in diameter, in which there is apparent boundary between HMUiO-66-NH₂ and COF-366-OH-Cu (**Figure 1f**). The detected lattice spacing of 1.98 nm is assigned to the (0 2 0) crystal plane of COF-366-OH-Cu, confirming the high crystallinity of MCH-3 (**Figure 1f**, insert image).^[42] Moreover, the high-angle annular dark-field scanning transmission electron microscopy (HAADF-STEM) and the corresponding energy dispersive X-ray (EDS) element mapping images clearly confirm the hetero-structure of MCH-3, in which the Zr element is densely distributed on the HMUiO-66-NH₂ core and Cu covers the entire hetero-structure (**Figure 1g**). In the HAADF-STEM, the MOF core is clearly calculated to be ~83 nm and the COF shell is only ~8.5 nm (**Figure 1g**). Moreover, the morphology of other MCH-X (X = 1, 2, 4) has been investigated and similar honeycomb-like hetero-structures were confirmed by the TEM, HAADF-STEM and elemental mapping measurements (**Figure 2**). Interestingly, the COF shell thickness change of MCH-X (X = 1-4) displays a volcano-like trend. In detail, MCH-1 has a COF coating thickness of ~10.5 nm, and it increases to ~14 nm for MCH-2 (**Figure 2a, b**). After that, the thickness decreases to ~8.5 nm for MCH-3 and further to ~8 nm for MCH-4, which might be affected by the varied surface synthetic-kinetics for different addition amounts of HMUiO-66-NH₂ in the MCH-X synthetic system (**Figure 2c, d**). Thus-obtained MCH-X (X = 1-4) with ultrathin COF shell thickness would be much beneficial for the exposing of active sites and electrocatalytic CO₂RR performance enhancement.

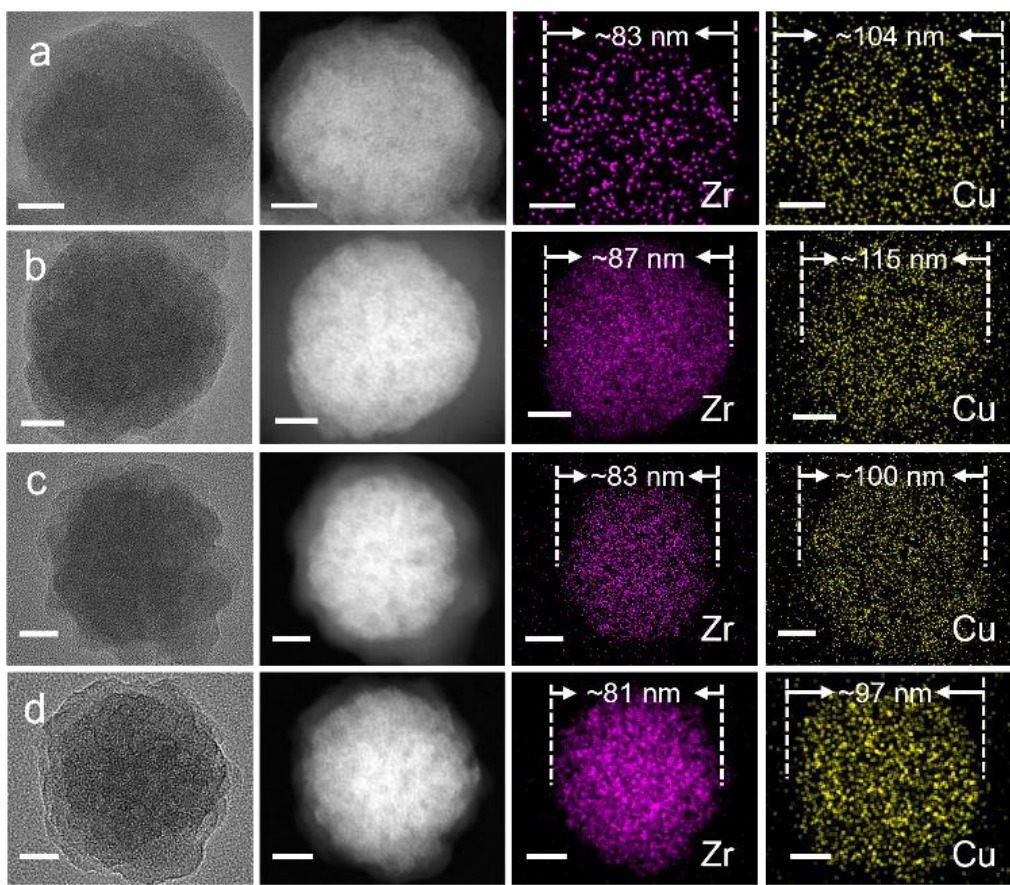


Figure 2. The TEM, HAADF-STEM and elemental mapping images of MCH-X (X = 1-4). (a) MCH-1. (b) MCH-2. (c) MCH-3. (d) MCH-4. The scale bar is 20 nm.

The successful combination COF-366-OH-Cu and HMUiO-66-NH₂ in the honeycomb-like morphology would inherit the porosity of them to achieve well-developed pore channels that might be beneficial for the mass transfer and CO₂ enrichment. To estimate the porosity of MCH-X (X = 1-4), N₂ and CO₂ sorption tests have been performed. The Brunner-Emmet-Teller surface area (S_{BET}) of HMUiO-66-NH₂, COF-366-OH-Cu are calculated to be 1139 and 303 cm² g⁻¹, respectively, based on the 77 K N₂ sorption results (**Figure 1d**). For MCH-X (X = 1-4), their S_{BET} values are calculated to be 685, 879, 947 and 762 cm² g⁻¹, respectively, which are all between HMUiO-66-NH₂ and COF-366-OH-Cu (**Figure S7 and Table S1**). Besides, the total pore volume (V_t) values for HMUiO-66-NH₂, COF-366-OH-Cu and MCH-X (X = 1-4) are detected to be 0.84, 0.17, 0.38, 0.59, 0.61 and 0.62 cm³ g⁻¹, respectively (**Figure 1d, S7 and Table S1**). Based on the S_{BET} and V_t results, we can get the conclusion

that MCH-X ($X = 1\text{-}4$) inherit the porosity of both HMUiO-66-NH₂ and COF-366-OH-Cu. This result is also supported by the pore size distribution curves of MCH-3 when compared with those of HMUiO-66-NH₂ and COF-366-OH-Cu (**Figure S8**). Taking MCH-3 as an example, the CO₂ adsorption capacity at 273 K ($\sim 42 \text{ cm}^3 \text{ g}^{-1}$) and 298 K ($\sim 27 \text{ cm}^3 \text{ g}^{-1}$) are higher than that of COF-366-OH-Cu and slightly lower than that of HMUiO-66-NH₂ (**Figure S9**). For MCH-X ($X = 1, 2, 4$), they all display close results to that of MCH-3 (**Figure S9**). Interestingly, the CO₂ adsorption enthalpy of MCH-3 is higher than that of HMUiO-66-NH₂ and COF-366-OH-Cu, indicating its more favored interaction with CO₂ (**Figure S10**). The high porosity combined with above-mentioned morphology would set fundamental basis for further applications like electrocatalytic CO₂RR.

2.2. Electrocatalytic CO₂ Reduction Performance

The obtained MCH-X ($X = 1\text{-}4$) with well-tuned honeycomb-like hetero-structure, high porosity, and inherited both advantages of COFs and MOFs might serve as desired platforms in electrocatalytic CO₂RR. To test the performance, the electrocatalysts were packaged in flow cells and tested in three-electrode electrochemical system. In this work, all the potentials are measured using a Ag/AgCl electrode and the results are reported relative to reversible hydrogen electrode (RHE).

Linear sweep voltammetry (LSV) curves present that HMUiO-66-NH₂, COF-366-OH-Cu and MCH-3 have total current density of $-187.8 \text{ mA cm}^{-2}$, $-374.4 \text{ mA cm}^{-2}$ and $-398.1 \text{ mA cm}^{-2}$ at -1.0 V , respectively (**Figure 3a**). Moreover, HMUiO-66-NH₂, COF-366-OH-Cu and MCH-3 all have much smaller current density in hydrogen evolution reaction (HER) than that in CO₂RR (**Figure S11**), suggesting the more favorable CO₂RR process than HER. In order to evaluate the product of electrocatalytic CO₂RR, the reactions were tested at various potentials and the products were characterized by gas chromatography (GC) and ¹H nuclear magnetic resonance spectroscopy (¹H NMR). Consequently, no liquid products were detected (**Figure S12**). For MCH-3, it shows a FE_{CH₄} of 76.7% at -1.0 V with a current density of $-398.1 \text{ mA cm}^{-2}$ and minor FE_{C₂H₄} (3.3%, -1.0 V) (**Figure 3a, b**). As comparison, HMUiO-66-NH₂ and COF-366-OH-Cu only exhibit FE_{CH₄} of 15.9% ($-187.8 \text{ mA cm}^{-2}$) and 37.5% ($-374.4 \text{ mA cm}^{-2}$) at -1.0 V , respectively, which supports the superiority of MCH-3 with honeycomb-like hetero-structure in electrocatalytic CO₂RR (**Figure 3a, b**). The achieved excellent

electrocatalytic CO₂RR performance (76.7%, -1.0 V) with high current density (-398.1 mA cm⁻²) is represented to be one of the best inorganic materials based electrocatalysts reported to date (**Table S2**). Notably, the FE_{CH₄} of MCH-3 keeps ~70% over a potential range from -0.9 V to -1.1 V (**Figure 3b**).

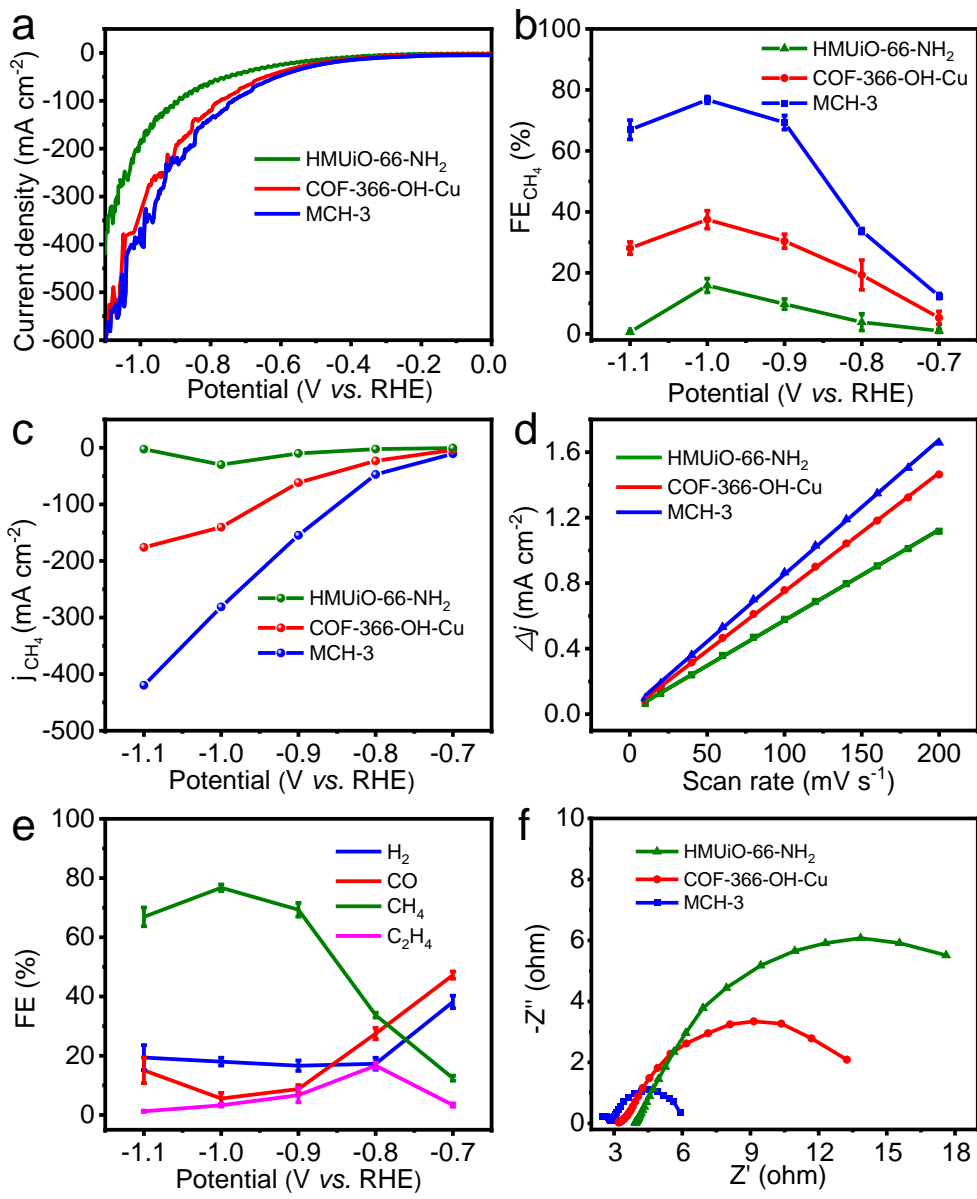


Figure 3. Electrocatalytic performances. (a) LSV curves of HMUiO-66-NH₂, COF-366-OH-Cu and MCH-3. (b) FE_{CH₄} calculated over potential range from -0.7 V to -1.1 V. (c) Partial CH₄ current density. (d) Capacitive current at 0.05 V as a function of scan rate for HMUiO-66-NH₂, COF-366-OH-Cu and MCH-3. (e) Faradaic efficiencies of MCH-3 at different applied potentials. (f) Nyquist plots of electrocatalysts over the frequency ranging from 100 kHz to 0.1 Hz at -1.0 V vs. RHE.

In addition, the electrochemical properties of MCH-X (X = 1, 2, 4) have also been evaluated. For MCH-1, it presents a FE_{CH₄} of 71.4% and FE_{C₂H₄} of 4.1% at -1.0 V (**Figure S13**). When they come to MCH-2 and MCH-4, they show decreased FE_{CH₄} and the values are 63.5% and 63.1% at -1.0 V (**Figure S14 and S15**). It is worth mentioning that MCH-3 could greatly inhibiting hydrogen production, which is far better than bare HMUiO-66-NH₂, COF-366-OH-Cu and other MCH-X (X = 1, 2, 4), probably due to the optimization of the ratio of HMUiO-66-NH₂ and COF-366-OH-Cu, which produces a lot of internal interfaces, thus greatly inhibiting hydrogen evolution. Besides, HMUiO-66-NH₂, COF-366-OH-Cu and MCH-3 present partial CH₄ current density of -29.8 mA cm⁻², -140.3 mA cm⁻² and -281.2 mA cm⁻² at -1.0 V, respectively (**Figure 3c**). The results show that the partial current density of MCH-3 is about twice higher than that of COF-366-OH-Cu (**Figure 3c**). Based on above-mentioned results, we select MCH-3 with the optimized property (FE_{CH₄}, 76.7%, -1.0 V) to further investigate other properties (**Figure 3e**).

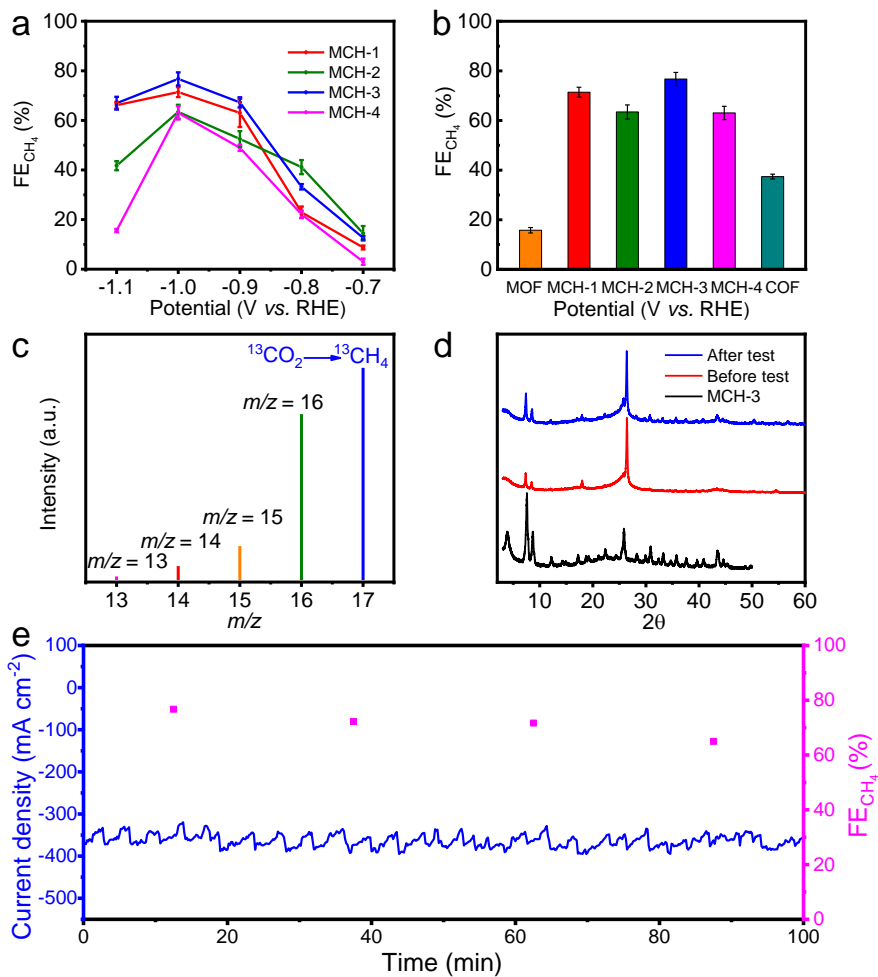


Figure 4. Electrocatalytic performances. (a) FE_{CH_4} of MCH-X (X = 1-4) at different applied potentials. (b) FE_{CH_4} of HMUiO-66-NH₂, COF-366-OH-Cu, MCH-X (X = 1-4) calculated at the potential of -1.0 V vs. RHE. (c) The mass spectra of $^{13}CH_4$ recorded under $^{13}CO_2$ atmosphere. (d) PXRD patterns of MCH-3 before and after electrochemical experiment. (e) Durability test of MCH-3 at the potential of -1.0 V vs. RHE.

Furthermore, electrochemical double-layer capacitance (C_{dl}) is calculated based on the electrochemical active surface area (ECSA) tests. The analysis displays that MCH-3 (8.21 mF cm⁻²) has higher C_{dl} value than that of HMUiO-66-NH₂ (5.53 mF cm⁻²), COF-366-OH-Cu (7.24 mF cm⁻²) (Figure

3d and S16), suggesting the advantages of MCH-3 with honeycomb-like hetero-structure that would possess more functional sites to promote the CO₂ electroreduction process.

In addition, the FE_{CH₄} of MCH-X (X = 1-4) at different applied potentials have been calculated. The results show that MCH-3 has the best performance among them and its highest FE_{CH₄} is achieved at -1.0 V (**Figure 4a**). Notably, the FE_{CH₄} (76.7%) of MCH-3 at -1.0 V is much higher than the contrast samples, in which the value is ~5 and ~2 times higher than HMUiO-66-NH₂ and COF-366-OH-Cu, respectively (**Figure 4a, b**). In electrocatalytic CO₂RR process, the determination of carbon source for products is vital to assess the validity of electrocatalyst. To test it, ¹³CO₂ was applied as substrate in isotopic experiment and the relative CO₂RR process was tested following similar procedures and conditions. Taking MCH-3 for instance, the products were characterized by GC and mass spectra. Specifically, peaks at *m/z* = 17, 29 and 30 are ascribed to ¹³CH₄, ¹³CO and ¹³C₂H₄, respectively, which supports the carbon sources of CH₄, CO and C₂H₄ (**Figure 4c and S17**). Moreover, electrochemical impedance spectroscopy (EIS) measurement has been conducted. Interestingly, the charge transfer resistance of HMUiO-66-NH₂, COF-366-OH-Cu and MCH-3 are evaluated to be 21.38 Ω, 9.74 Ω and 3.26 Ω, respectively (**Figure 3f and S18**), implying that MCH-3 would exhibit faster electron transfer than that of HMUiO-66-NH₂ and COF-366-OH-Cu to result in largely improved performance. Besides, we have calculated the energy efficiency at different potentials, the energy efficiency of MCH-3 could reach up to 36.5% at -1.0 V, which is ~2 and ~5 times higher than that of COF-366-OH-Cu (17.8%, -1.0 V) and HMUiO-66-NH₂ (7.5%, -1.0 V), respectively (**Figure S19**).

Stability is vital to assess the electrocatalytic CO₂RR property as it is related to the durability of electrocatalysts. The longtime durability test of MCH-3 was evaluated at -1.0 V by chronoamperometric curves. After 90 min, the FE_{CH₄} can be remained higher than 65.0% with current density of about -359.4 mA cm⁻² (**Figure 4e**). After test, the PXRD test showed that the patterns of MCH-3 matched well with state before test (**Figure 4d**). Besides, the TEM measurements of MCH-3 after electrocatalytic CO₂RR showed unchanged honeycomb-like hetero-structure, which verified the high stability (**Figure S20**).

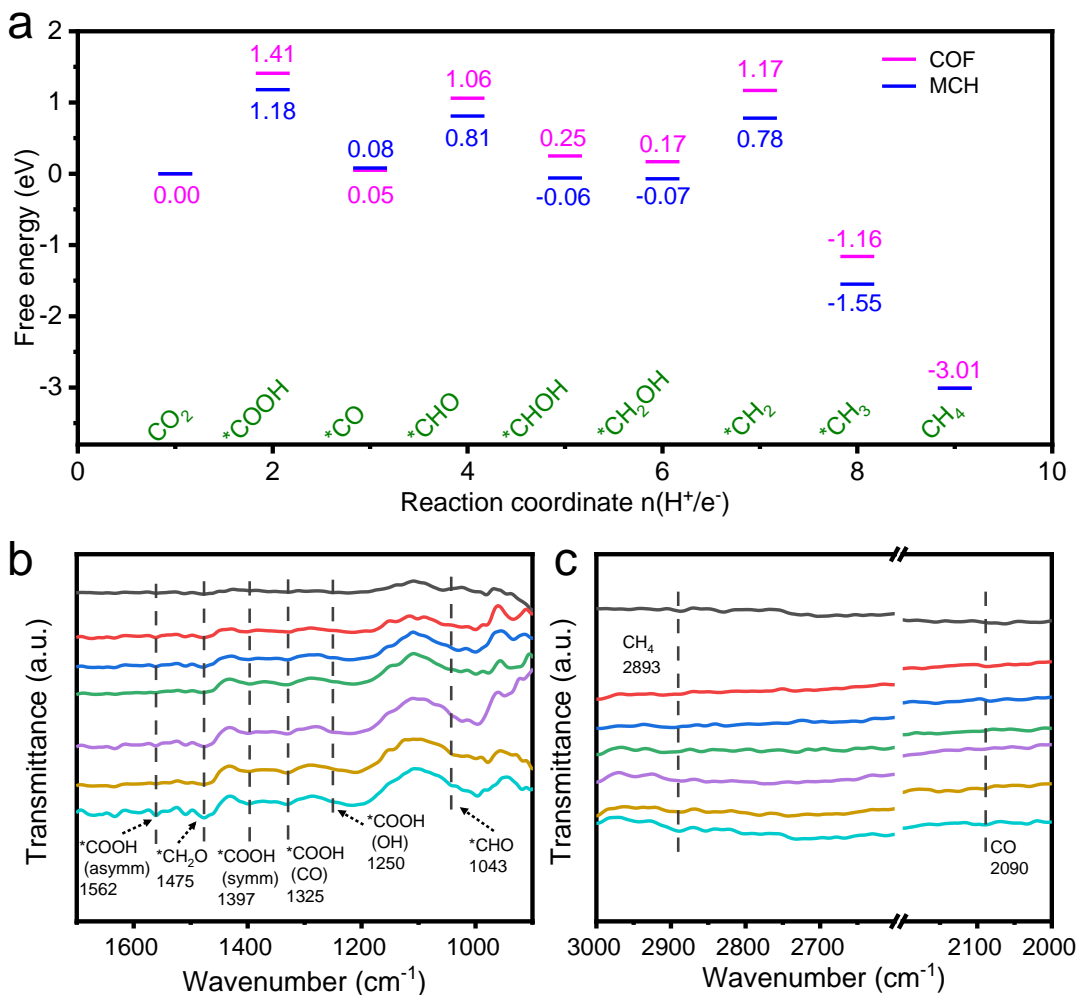


Figure 5. DFT calculations and CO₂RR and in-situ ATR-FTIR spectra. (a) Free energy profiles for CO₂-to-CH₄ reaction pathway on COF and MCH-3, respectively. (b) In-situ ATR-FTIR spectra of MCH-3 during the electrochemical CO₂RR (range, 1700 cm⁻¹ to 900 cm⁻¹). (c) In-situ ATR-FTIR spectra of MCH-3 during the electrochemical CO₂RR (range, 3000 cm⁻¹ to 2000 cm⁻¹).

2.3. Investigating the Structure-Function Relationships

In general, the formation of CH₄ has two possible reaction pathways including *HCOOH pathway or *CO pathway as supported by the reported literatures.^[50-52] As mentioned above, the main CO₂ reduction products of COF-366-OH-Cu and MCH-3 are CH₄ and CO, and their CO production decreases following the formation of CH₄. Thus, it could be deduced that the *CO pathways are

occurred on both COF-366-OH-Cu and MCH-3, including the generation of intermediates such as *CO₂, *COOH, *CO, *CHO, *CHOH, *CH₂OH, *CH₂, *CH₃ and *CH₄, coupling with the following multi-step proton-electron transfer processes. Besides, DFT calculations are subsequently conducted to reveal the detailed free energy profiles for each reaction coordinate during the CO₂-to-CH₄ pathways and summarized (**Figure 5a, Figure S21 and S22**). During the whole reaction pathway, there reaction steps are not spontaneous ($\Delta G > 0$), including the formation of *COOH, *CHO and *CH₂. The formation of *COOH serves as the rate-determining step ($\Delta G = 1.18$ eV) (**Figure 5a**). Interestingly, the free energy value of MCH-3 for the rate-determining step is lower than that of COF-366-OH-Cu, indicating the positive effect of MOF on the vital reaction step. Besides, the following steps are also largely affected by the hybridization of MOF in MCH-3, in which their free energy values are lower than those of COF-366-OH-Cu (**Figure 5a**). It seems that MOF would provide an extra stabilization effect for the intermediates to decrease the free energy. To further ascertain the intermediates during the CO₂RR process, in-situ ATR-FTIR measurements have been performed (**Figure 5b**). The bands at 1250 cm⁻¹, 1325 cm⁻¹, 1397 cm⁻¹, and 1562 cm⁻¹ in the spectra are assigned to the OH deformation, C-O stretch, symmetric and asymmetric stretch of *COOH intermediate, respectively.^[16] These important intermediates are regarded as the key intermediates for the formation of CH₄. Moreover, the signals appeared at 1043 cm⁻¹, 1475 cm⁻¹ and 2090 cm⁻¹ can be assigned to *CHO, *CH₂O and CO (*CO), respectively (**Figure 5b, c**),^[16] which are the crucial intermediates for CO₂RR to CH₄ that can further prove the possible mechanism.

To further identify the actual reactive sites, the catalytic mechanism of Zr-MOF has been calculated by DFT calculations. As shown in **Figure S23**, each Zr center is highly coordinated with eight O atoms and it presents repulsion behavior for *COOH adsorption, indicating the pristine and coordinated Zr-centers in UiO-66-NH₂ cannot provide extra coordination space for CO₂ or other intermediates during the CO₂RR process. However, the experimental result shows that HMUiO-66-NH₂ has a low activity in generation of CH₄, which drives us to further explore its possible interaction like defective effect on the CO₂RR process. To study it, the defective tests and DFT calculations have been conducted. Firstly, NH₃ temperature programmed desorption (NH₃-TPD) test, a kind of defect evolution technique, has been performed to determine the defects of HMUiO-66-NH₂. Based on the NH₃-TPD result, HMUiO-66-NH₂ has three main peaks centered at 120 °C, 180 °C and 350 °C, which

can be ascribed to the physical sorption of NH₃, Lewis acid sites (e.g., unsaturated metal sites) and Brønsted acid sites (e.g., uncoordinated carboxyl groups), respectively (**Figure S24**).^[53,54] Inspired by these results, we further remove one coordinated OCHO ligand to create the defective Zr sites in DFT calculations, which can be existed under the operation condition. In general, there are two possible reaction pathways including *CO₂-*OCHO^[55] and typical *CO₂-*COOH routes.^[50-52] The free energy profiles of the CH₄ production along with the *CO₂-*OCHO route are illustrated in **Figure S25**. Apparently, the re-formation of *OCHO from *CO₂ is much energetic favorable comparing with the reaction path from *CO₂ to *COOH (**Figure S26**). Therefore, *CO₂-*OCHO pathway is the possible route for HMUiO-66-NH₂. Comparing with the free energy change on the Cu sites, the rate-determining step from *OCHO to *OCHOH (1.81 eV) of HMUiO-66-NH₂ is much larger than all the elemental steps on Cu sites. Therefore, we conclude here that the active sites for CO₂RR-to-CH₄ are mainly Cu sites and the reaction rate on Zr sites is relatively lower, which can be also proved by the experimental results. Besides, DFT calculations have also been carried out to reveal the detailed free energy profiles for HER on Cu sites. The results show that the rate-determining step from H⁺ + e⁻ to *H (1.95 eV) is much larger than that of CO₂RR (1.18 eV) on Cu sites (**Figure S27**), which is also proved by much smaller current density in HER than that in CO₂RR as mentioned above. Therefore, the introduction of HMUiO-66-NH₂ can not only serve as a kind of powerful template to grow ultrathin COF layers but also facilitate CO₂ adsorption/activation, stabilize intermediates, and conquer the energy barrier of rate-determining step to largely improve the electrocatalytic CO₂RR performance.

3. Conclusion

In summary, we have successfully designed a series of honeycomb-like porous crystalline hetero-electrocatalysts (MCH-X, X = 1-4) through an epitaxial growth strategy. Thus-obtained hetero-structures possess unique honeycomb-like morphology, large surface area, high stability, and well-exposed active sites, and rich inner-interface interaction that are much beneficial for electrocatalytic CO₂RR to CH₄. Best of them, the MCH-3 showed greatly inhibited H₂ evolution, excellent current density (-398.1 mA cm⁻²), and superior FE_{CH₄} (76.7%) to physical mixture (38.0%), MOF@COF

without honeycomb-like morphology (47.7%), bare COF (37.5%) and MOF (15.9%) at -1.0 V. Noteworthy, the achieved excellent electrocatalytic CO₂RR performance (76.7%, -1.0 V) with high current density (-398.1 mA cm⁻²) is represented to be one of the best electrocatalytic CO₂RR catalysts reported to date. Moreover, based on the DFT calculations and various characterizations, the vital roles of MOFs in facilitating CO₂ adsorption/activation, stabilizing intermediates, and conquering the energy barrier of rate-determining step have been intensively studied. The electro-catalysts based on such powerful hybrid materials designed by combining porous defective MOF with catalytically active COF offer a high possibility to achieve highly efficient electrocatalytic CO₂RR system, which might also expand the scope of porous crystalline materials in this field.

4. Experimental Section

Synthesis of HMUiO-66-NH₂: The synthesis of HMUiO-66-NH₂ followed previously reported method^[47]. Detailly, F127 (2.5 g) was dissolved in 150 mL deionized water, the mixture was stirred to form a homogeneous solution. Then, HAc (20 mL) and NaClO₄·H₂O (7.5 g) were added. Subsequently, Zr(NO₃)₄·5H₂O (115.6 mg, 0.5 mmol) and BDC-NH₂ (50 mg, 0.28 mmol) were added into the above mixture. Then, the mixture was stirred at 40 °C for 12 h. The resultant solid was isolated by centrifugation and washed with water and DMF for several times. The as-synthesized sample was soaked in ethanol for 2 days at 60 °C to remove the F127 template, and the ethanol was renewed after one day. Finally, the product was dried at 60 °C under vacuum.

Synthesis of Cu-TAPP: The synthesis of Cu-TAPP follows previously reported method^[42]. In detail, 5,10,15,20-tetrakis (4-aminophenyl)-21H,23H-psorphine (H₂-TAPP) (200 mg, 0.3 mmol) and Cu(OAc)₂·H₂O (239.58 mg, 1.2 mmol) were mixed in 250 mL three-neck round bottomed flask. After purification with N₂ for 3 times, a mixed solution of methanol (20 mL), chloroform (90 mL) and DMF (30 mL) was added. The flask was heated at 80 °C under N₂ for 24 h. After cooling to room temperature, the solution was transferred into a separatory funnel and washed with water (3 × 100

mL). Then, the solution was collected through rotary evaporation to afford dark purple solid (Cu-TAPP, ~180 mg, ~82% yield).

Synthesis of COF-366-OH-Cu: The synthesis of COF-366-OH-Cu follows previously reported method^[42]. 2,5-dihydroxyterephthalaldehyde (DHA) (13.3 mg, 0.08 mmol) and tetra(p-aminophenyl)porphyrin (Cu-TAPP) (30.0 mg, 0.04 mmol) were added in a tube, using the mixed solution of dichlorobenzene (1 mL) and ethanol (1 mL) as the solvent. This mixture was sonicated for 10-15 min to achieve homogenous dispersion. After that, 6 M HAc (0.2 mL) was added in the tube and sonicated for another 5 min. The tube was then flash frozen at 77 K (liquid N₂ bath) and degassed by three freeze-pump-thaw cycles. The tube was sealed off and then heated at 120 °C for 3 days. The COF powders were filtered out, washed with THF and dried under vacuum at 120 °C for 12 h to obtain purple powder.

Synthesis of HMUiO-66-NH₂@COF-366-OH-Cu (MCH-X) (X = 1-4): Cu-TAPP (30 mg, 0.04 mmol), DHA (13.3 mg, 0.08 mmol), HMUiO-66-NH₂ (10, 30, 50 and 70 mg), (1 mL), dichlorobenzene (1 mL), ethanol (1 mL) and 6 M aqueous HAc (200 µL) were mixed in a Pyrex tube (o.d × length, 19 × 65 mm). Then, the subsequent synthetic procedures are similar to that of COF-366-OH-Cu. The obtained samples were named from MCH-1 to MCH-4, in which X stands for the sample obtained from different MOFs doses in the MCH synthesis.

Supporting Information

Supporting Information is available from the Wiley Online Library or from the author.

Acknowledgements

This article is protected by copyright. All rights reserved.

This work was financially supported by the NSFC (Grants 22171139, 22225109, 21871141, 21871142, 21901122 and 22071109), Guangdong Basic and Applied Basic Research Foundation (No.2021A1515110429), and Postdoctoral Innovation Talent Support Program (No. BX20220116).

Yi-Lu Yang, Yi-Rong Wang and Long-Zhang Dong contributed equally to this work.

Conflict of Interest

The authors declare no conflict of interest.

Author contributions

Y.-Q. L., Y. C. and Y.-L. Y. conceived the idea. Y.-L. Y. designed the experiments, Y.-R. W. and L.-Z. D. collected and analyzed the data. Q. L., L. Z., S.-N. S. H.-M. D. and S.-L. L assisted with the experiments and characterizations. Y.-L. Y. wrote the manuscript. All authors discussed the results and commented on the manuscript.

Received: ((will be filled in by the editorial staff))

Revised: ((will be filled in by the editorial staff))

Published online: ((will be filled in by the editorial staff))

References

- [1] S. Diercks Christian, M. Yaghi Omar, *Science* **2017**, *355*, eaal1585.
- [2] K. Geng, T. He, R. Liu, S. Dalapati, K. T. Tan, Z. Li, S. Tao, Y. Gong, Q. Jiang, D. Jiang, *Chem. Rev.* **2020**, *120*, 8814.
- [3] R.-R. Liang, S.-Y. Jiang, R.-H. A, X. Zhao, *Chem. Soc. Rev.* **2020**, *49*, 3920.

This article is protected by copyright. All rights reserved.

- [4] M. S. Lohse, T. Bein, *Adv. Funct. Mater.* **2018**, *28*, 1705553.
- [5] Y. Yang, X. He, P. Zhang, Y. H. Andaloussi, H. Zhang, Z. Jiang, Y. Chen, S. Ma, P. Cheng, Z. Zhang, *Angew. Chem. Int. Ed.* **2020**, *59*, 3678.
- [6] H. Ma, B. Liu, B. Li, L. Zhang, Y.-G. Li, H.-Q. Tan, H.-Y. Zang, G. Zhu, *J. Am. Chem. Soc.* **2016**, *138*, 5897.
- [7] P.-F. Wei, M.-Z. Qi, Z.-P. Wang, S.-Y. Ding, W. Yu, Q. Liu, L.-K. Wang, H.-Z. Wang, W.-K. An, W. Wang, *J. Am. Chem. Soc.* **2018**, *140*, 4623.
- [8] C. Li, Q. Li, Y. V. Kaneti, D. Hou, Y. Yamauchi, Y. Mai, *Chem. Soc. Rev.* **2020**, *49*, 4681.
- [9] Y. Zeng, R. Zou, Y. Zhao, *Adv. Mater.* **2016**, *28*, 2855.
- [10] H. Fan, A. Mundstock, A. Feldhoff, A. Knebel, J. Gu, H. Meng, J. Caro, *J. Am. Chem. Soc.* **2018**, *140*, 10094.
- [11] J. Li, X. Jing, Q. Li, S. Li, X. Gao, X. Feng, B. Wang, *Chem. Soc. Rev.* **2020**, *49*, 3565.
- [12] C. R. DeBlase, K. E. Silberstein, T.-T. Truong, H. D. Abruña, W. R. Dichtel, *J. Am. Chem. Soc.* **2013**, *135*, 16821.
- [13] M.-D. Zhang, D.-H. Si, J.-D. Yi, S.-S. Zhao, Y.-B. Huang, R. Cao, *Small* **2020**, *16*, 2005254.
- [14] G. C. Dubed Bandomo, S. S. Mondal, F. Franco, A. Bucci, V. Martin-Diaconescu, M. A. Ortúñoz, P. H. van Langevelde, A. Shafir, N. López, J. Lloret-Fillol, *ACS Catal.* **2021**, *11*, 7210.
- [15] C. S. Diercks, S. Lin, N. Kornienko, E. A. Kapustin, E. M. Nichols, C. Zhu, Y. Zhao, C. J. Chang, O. M. Yaghi, *J. Am. Chem. Soc.* **2018**, *140*, 1116.
- [16] Y.-R. Wang, H.-M. Ding, X.-Y. Ma, M. Liu, Y.-L. Yang, Y. Chen, S.-L. Li, Y.-Q. Lan, *Angew. Chem. Int. Ed.* **2022**, *61*, e202114648.
- [17] Y.-L. Yang, Y.-R. Wang, G.-K. Gao, M. Liu, C. Miao, L.-Y. Li, W. Cheng, Z.-Y. Zhao, Y. Chen, Z. Xin, S.-L. Li, D.-S. Li, Y.-Q. Lan, *Chin. Chem. Lett.* **2022**, *33*, 1439.

- [18] H.-J. Zhu, M. Lu, Y.-R. Wang, S.-J. Yao, M. Zhang, Y.-H. Kan, J. Liu, Y. Chen, S.-L. Li, Y.-Q. Lan, *Nat. Commun.* **2020**, *11*, 497.
- [19] X. Zhao, P. Pachfule, A. Thomas, *Chem. Soc. Rev.* **2021**, *50*, 6871.
- [20] M. Liu, Y.-R. Wang, H.-M. Ding, M. Lu, G.-K. Gao, L.-Z. Dong, Q. Li, Y. Chen, S.-L. Li, Y.-Q. Lan, *Sci. Bull.* **2021**, *66*, 1659.
- [21] Y. Zhu, X. Yang, C. Peng, C. Priest, Y. Mei, G. Wu, *Small* **2021**, *17*, 2005148.
- [22] R.-X. Yang, Y.-R. Wang, G.-K. Gao, L. Chen, Y. Chen, S.-L. Li, Y.-Q. Lan, *Small Structures* **2021**, *2*, 2100012.
- [23] S. Yuan, L. Feng, K. Wang, J. Pang, M. Bosch, C. Lollar, Y. Sun, J. Qin, X. Yang, P. Zhang, Q. Wang, L. Zou, Y. Zhang, L. Zhang, Y. Fang, J. Li, H.-C. Zhou, *Adv. Mater.* **2018**, *30*, 1704303.
- [24] L. Jiao, J. Y. R. Seow, W. S. Skinner, Z. U. Wang, H.-L. Jiang, *Mater. Today* **2019**, *27*, 43.
- [25] H. L. Nguyen, F. Gándara, H. Furukawa, T. L. H. Doan, K. E. Cordova, O. M. Yaghi, *J. Am. Chem. Soc.* **2016**, *138*, 4330.
- [26] A. Kuc, M. A. Springer, K. Batra, R. Juarez-Mosqueda, C. Wöll, T. Heine, *Adv. Funct. Mater.* **2020**, *30*, 1908004.
- [27] X. Zhang, B. Wang, A. Alsalme, S. Xiang, Z. Zhang, B. Chen, *Coord. Chem. Rev.* **2020**, *423*, 213507.
- [28] X. Liu, M. Hu, M. Wang, Y. Song, N. Zhou, L. He, Z. Zhang, *Biosens. Bioelectron.* **2019**, *123*, 59.
- [29] S. Zhang, W. Xia, Q. Yang, Y. Valentino Kaneti, X. Xu, S. M. Alshehri, T. Ahamad, M. S. A. Hossain, J. Na, J. Tang, Y. Yamauchi, *Chem. Eng. J.* **2020**, *396*, 125154.
- [30] F.-M. Zhang, J.-L. Sheng, Z.-D. Yang, X.-J. Sun, H.-L. Tang, M. Lu, H. Dong, F.-C. Shen, J. Liu, Y.-Q. Lan, *Angew. Chem. Int. Ed.* **2018**, *57*, 12106.

- [31] W. Sun, X. Tang, Q. Yang, Y. Xu, F. Wu, S. Guo, Y. Zhang, M. Wu, Y. Wang, *Adv. Mater.* **2019**, *31*, 1903176.
- [32] Y. Peng, M. Zhao, B. Chen, Z. Zhang, Y. Huang, F. Dai, Z. Lai, X. Cui, C. Tan, H. Zhang, *Adv. Mater.* **2018**, *30*, 1705454.
- [33] Y. Li, M. Karimi, Y.-N. Gong, N. Dai, V. Safarifard, H.-L. Jiang, *Matter* **2021**, *4*, 2230.
- [34] M. Li, S. Qiao, Y. Zheng, Y. H. Andaloussi, X. Li, Z. Zhang, A. Li, P. Cheng, S. Ma, Y. Chen, *J. Am. Chem. Soc.* **2020**, *142*, 6675.
- [35] N. Zhou, Y. Ma, B. Hu, L. He, S. Wang, Z. Zhang, S. Lu, *Biosens. Bioelectron.* **2019**, *127*, 92.
- [36] X. Liu, S. Zhang, G. Feng, Z.-G. Wu, D. Wang, M. D. Albaqami, B. Zhong, Y. Chen, X. Guo, X. Xu, Y. Yamauchi, *Chem. Mater.* **2021**, *33*, 1657.
- [37] J. Fu, S. Das, G. Xing, T. Ben, V. Valtchev, S. Qiu, *J. Am. Chem. Soc.* **2016**, *138*, 7673.
- [38] M. Cai, Y. Li, Q. Liu, Z. Xue, H. Wang, Y. Fan, K. Zhu, Z. Ke, C. Y. Su, G. Li, *Adv Sci (Weinh)* **2019**, *6*, 1802365.
- [39] C. Guo, F. Duan, S. Zhang, L. He, M. Wang, J. Chen, J. Zhang, Q. Jia, Z. Zhang, M. Du, *J. Mater. Chem. A* **2022**, *10*, 475.
- [40] B. Deng, M. Huang, K. Li, X. Zhao, Q. Geng, S. Chen, H. Xie, X. Dong, H. Wang, F. Dong, *Angew. Chem. Int. Ed. Engl.* **2022**, *61*, e202114080.
- [41] G. Yuan, L. Tan, P. Wang, Y. Wang, C. Wang, H. Yan, Y.-Y. Wang, *Cryst. Growth Des.* **2021**, *22*, 893.
- [42] S. Kandambeth, D. B. Shinde, M. K. Panda, B. Lukose, T. Heine, R. Banerjee, *Angew. Chem. Int. Ed. Engl.* **2013**, *52*, 13052.
- [43] M. Lu, J. Liu, Q. Li, M. Zhang, M. Liu, J. L. Wang, D. Q. Yuan, Y. Q. Lan, *Angew. Chem. Int. Ed. Engl.* **2019**, *58*, 12392.

- [44] M. Chen, H. Li, C. Liu, J. Liu, Y. Feng, A. G. H. Wee, B. Zhang, *Coord. Chem. Rev.* **2021**, 435.
- [45] Y. Chen, D. Yang, B. Shi, W. Dai, H. Ren, K. An, Z. Zhou, Z. Zhao, W. Wang, Z. Jiang, *J. Mater. Chem. A* **2020**, 8, 7724.
- [46] J. Tang, C. Su, Z. Shao, *Small Methods* **2021**, 5, e2100945.
- [47] K. Li, J. Yang, J. Gu, *Chem. Mater.* **2021**, 33, 2198.
- [48] C. Gomes Silva, I. Luz, F. X. Llabrés i Xamena, A. Corma, H. García, *Chemistry – A European Journal* **2010**, 16, 11133.
- [49] M. S. Xie, B. Y. Xia, Y. Li, Y. Yan, Y. Yang, Q. Sun, S. H. Chan, A. Fisher, X. Wang, *Energ. Environ. Sci.* **2016**, 9, 1687.
- [50] H. Zhang, X. Chang, J. G. Chen, W. A. Goddard, B. Xu, M.-J. Cheng, Q. Lu, *Nat. Commun.* **2019**, 10, 3340.
- [51] D. Ren, B. S.-H. Ang, B. S. Yeo, *ACS Catal.* **2016**, 6, 8239.
- [52] C. G. Morales-Guio, E. R. Cave, S. A. Nitopi, J. T. Feaster, L. Wang, K. P. Kuhl, A. Jackson, N. C. Johnson, D. N. Abram, T. Hatsukade, C. Hahn, T. F. Jaramillo, *Nat. Catal.* **2018**, 1, 764.
- [53] Y. Chen, Y.-J. Chen, Y. Qi, H.-J. Zhu, X. Huang, Y.-R. Wang, R.-X. Yang, Y.-H. Kan, S.-L. Li, Y.-Q. Lan, *Chem* **2021**, 7, 463.
- [54] M. I. Gonzalez, A. B. Turkiewicz, L. E. Darago, J. Oktawiec, K. Bustillo, F. Grandjean, G. J. Long, J. R. Long, *Nature* **2020**, 577, 64.
- [55] L. Han, S. Song, M. Liu, S. Yao, Z. Liang, H. Cheng, Z. Ren, W. Liu, R. Lin, G. Qi, X. Liu, Q. Wu, J. Luo, H. L. Xin, *J. Am. Chem. Soc.* **2020**, 142, 12563.

A series of honeycomb-like MOF@COF hetero-structures with integrated porous MOF-template and ultrathin COF-coating have been synthesized and successfully applied in efficient CO_2 electroreduction to CH_4 .

Yi-Lu Yang^{1‡}, Yi-Rong Wang^{1‡}, Long-Zhang Dong^{1‡}, Qi Li², Lei Zhang¹, Jie Zhou¹, Sheng-Nan Sun¹, Hui-Min Ding², Yifa Chen^{1*}, Shun-Li Li¹ & Ya-Qian Lan¹

Honeycomb-like Porous Crystalline Hetero-electrocatalyst for Efficient Electrocatalytic CO_2 Reduction

